A Miniature Triaxial Fiber Optic Force Sensor for Flexible Ureteroscopy

Yinan Deng, Tangwen Yang, *Member, IEEE*, Shaotao Dai, and Guoli Song

Abstract*—*Objective: **Design and evaluate a miniature triaxial fiber optic sensor which is integrated into the confined space at the tip of a flexible ureteroscope to measure the contact force during ureteroscopy. *Methods:* A notched flexure of multilayer continuous beams is deliberately designed to modulate the sensor sensitivity to axial stiffness but not to lateral bending and torsion, and to avoid the crosstalk between axial and lateral forces. Its structure parameters are optimized by the finite element method to meet the needs of miniaturization and performance. A linear decoupled model based on the singular value decomposition algorithm is proposed to accurately compute the forces from the wavelength shifts of fiber Bragg grating. *Results*: Experimental results show that in the axial direction the sensor has a range of 0-4 N with a resolution of 0.014 N, and in the lateral direction it has a resolution of 0.011 N within the range of -2 N to 2 N, and is able to provide accurate measurement with an error of less than 2%. *Conclusion:* Primary tests show the excellent competence of the sensor to measure the interactive force at the ureteroscope tip and to discriminate objects, validating its reliability and robustness.**

***Index Terms*—Force sensor, flexible ureteroscope, fiber Bragg grating, finite element method, singular value decomposition algorithm.**

I. Introduction

UROLOGICAL stone disease remains prevalent in the last decades [1], [2]. The data from hospitals show an increase in the number of flexible ureteroscopy (FURS) used in the treatment of stone disease, especially for larger stone, bleeding diathesis and pediatric patients [3], [4]. The ureteroscope is long, flexible, and is manually inserted into the urinary tract. This deprives the tactile perception of surgeons who are accustomed to having in open surgery. Lately, robotic ureteroscopy [5] has received burgeoning interest in the community of urological surgery due to the improvement of ergonomics, and the shorter learning curve [6], [7]. The flexible ureteroscope is steered by a robotic manipulator, which is remotely controlled by surgeon through a joystick. The same problem arises, that is, the surgeon has no interactive force information at the tip of ureteroscope, which may cause catastrophic injury of healthy tissue and even ureteroscope damage. Therefore, force feedback is crucial to ensure the ureteroscopy safety and outcome [8], [9].

Unfortunately, to date no sensor has been featured to measure the force at the tip of a flexible ureteroscope. Generally, the size of the conventional force sensors, such as strain gauge [10], piezoresistive transducer [11], is too large to be integrated into the small, confined space at the ureteroscope tip. In the last decade, fiber optic sensing technology was thus used to design force sensor due to its unique properties of miniaturization and biocompatibility. Some fiber optic sensors have been designed to use in cardiac catheterization procedures [12] and surgical palpation [13]. Frequently, two types of fiber optic sensors are used. One is based on the modulation of the light intensity, which is varying with the flexure deformation caused by external force [14], [15]. The other one uses the interferometric intensity or phase modulation. For example, the Fabry-Perot interferometer (FPI) was used to measure the force at the tip of needles [16], [17] and cardiac catheters [18]. The FPI sensor has better sensitivity in the axial direction than that in the lateral. However, the performance of these force sensors is deteriorated by light intensity fluctuation and phase discontinuity.

Fiber Bragg gating (FBG) modulates changes in wavelength of light associated with the Bragg resonance condition. It is just a few millimeters long, and the Bragg grating is inscribed in series on the optical fiber, which can be as small as hundreds of microns, and thus enables the miniaturization design of a sensor. Meanwhile, the wavelength encoding makes it immune to light intensity fluctuations [19]. Recently, FBG based sensor appears to be promising in the force measurement at the tip of surgical instrument [8], [20]–[23]. He *et al.* [20] developed a sub-millimetric force sensor with high resolution for retinal microsurgery. Four FBGs are used and integrated with an ophthalmological micro-pick instrument. To measure the force at the tip of ablation catheter, Li *et al.* [21] designed a triaxial sensor with a diameter of 4 *mm* and five FBGs. Four of the five fibers with FBG inscribed are fixed inside the grooves on the elliptical arc spherical hinge of an alloy flexure, but these FBGs are exposed to air, making them prone to damage. In

Manuscript received July 25, 2020; revised September 16, 2020; accepted October 18, 2020. Date of publication October 28, 2020; date of current version July 19, 2021. This work was supported in part by the State's Key Project of Research and Development Plan under Grants 2017YFB1302802 and 2017YFB0902302, and the National Natural Science Foundation of China under Grant 61375109. *(Corresponding author: Tangwen Yang.)*

Yinan Deng is with the Institute of Information Science and the Beijing Key Laboratory of Advanced Information Science and Network Technology, Beijing Jiaotong University.

Tangwen Yang is with the Institute of Information Science and the Beijing Key Laboratory of Advanced Information Science and Network Technology, Beijing Jiaotong University, Beijing 100044, China (e-mail: twyang@bjtu.edu.cn).

Shaotao Dai is with the School of Electrical Engineering, Beijing Jiaotong University.

Guoli Song is with the State Key Laboratory of Robotics, Shenyang Institute of Automation.

Digital Object Identifier 10.1109/TBME.2020.3034336

TABLE I
THE REQUIREMENTS OF FORCE SENSOR

Characteristics	Specifications
Dimension	1.2 mm (working channel size)$\leqslant$ Sensor diameter $\leqslant$3.0 mm (ureteroscope size)
Force range	$F_z \leqslant 4$ N, $\lvert F_x$ or $F_y \rvert \leqslant 2$ N
Resolution	0.02 N

[22], the sensor was developed with 3D printed resin flexure, which has a hollow cylinder with inner elliptical cavity and a hybrid elastomer, to replace the previous hinge and protect the FBGs. Gao *et al*. [23] designed a force sensor with parallel flexure hinges for catheter ablation. The flexure hinges are used to achieve the stiffness balance at the axial and lateral directions. But the hinges structure is complicated to fabricate. What's more, it is not small enough to integrate into the ureteroscope tip.

In this paper, a compact, triaxial force sensor is devised with fewer FBGs, to accommodate to small confined space. It is integrated into the tip of a flexible ureteroscope to measure the force applied to the wall of urinary tract, or the renal stone. In Section II, the force sensor is developed with four FBGs, which are fixed on a notched flexure with multilayer continuous beams, and the flexure parameters are optimized by finite element analysis (FEA). In Section III, the singular value decomposition (SVD) method is introduced to establish a linear decoupled model to compute the interaction force from the wavelength shifts of the FBGs. Finally, a sensor prototype is fabricated and calibrated, and tests are done to assess its performance and capability.

II. SENSOR DESIGN

A. Design Requirements

Flexible ureteroscopes usually have four channels: two channels for imaging and illumination, deflection mechanism channel and working channel. To measure the interaction force at the ureteroscope tip, we presume here the sensor is placed inside the working channel of flexible ureteroscope, for purpose of concept proof. Therefore, the requirements to design this sensor, given in Table I, are largely restricted by the size of the ureteroscope working channel, and the forces applied to the ureteroscope tip. As the sensor is assembled into the working channel of the flexible ureteroscope (PolyDiagnost GmbH), its size should be smaller than that of the ureteroscope but larger than the diameter of the working channel. Furthermore, the maximal force in the axial direction F_z is set to be 4 N, and the lateral forces F_x and F_y are confined to be the interval of $[-2\,\text{N}, 2\,\text{N}]$, in terms of the clinical data from patients [24], [25]. Meanwhile, the force resolution should be less than 0.02 N to ensure the sensor sensitivity and the procedure safety. Apart from these specifications, biocompatibility, electromagnetic compatibility, and sterilizing facilitation should be considered as well for the force sensor as a kind of medical device for use in ureteroscopy.

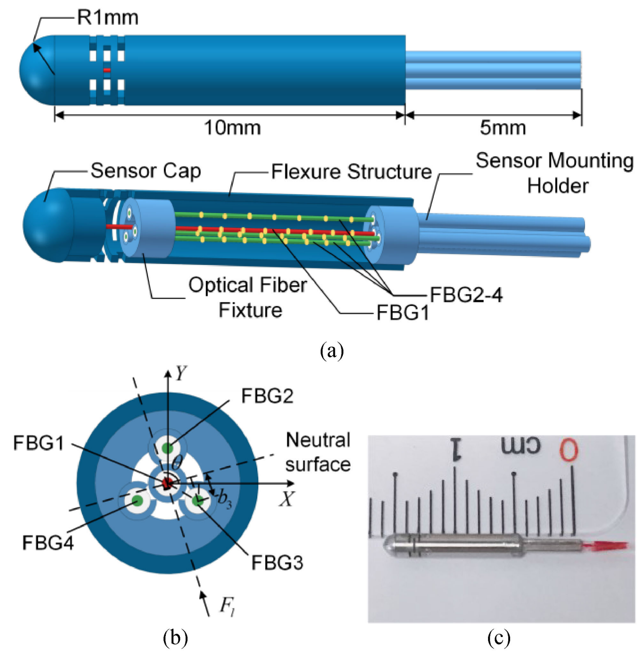

Fig. 1. The schematic diagram of a triaxial fiber optic force sensor for flexible ureteroscope. (a) structure and assembly overview; (b) cross-section; (c) prototype.

B. Force Sensor Design

To meet the above requirements, a fiber optic force sensor is devised here, and its configuration and assembly is illustrated in Fig. 1. This force sensor comprises of four FBGs and four mechanical parts, namely, a flexure, an optical fiber fixture, a sensor mounting holder and a sensor cap. The four FBGs are strain gauges which are inscribed on four optic fibers to generate light wavelength shifts as external force is applied to the gauges. The FBG1-inscribed optic fiber (the red line) is placed along the neutral axis of the force sensor, and is used to measure the axial force. Its proximal and distal ends are glued by epoxy to the internal undercuts of the mounting holder and the sensor cap. The other three identical FBGs (the green lines) are distributed peripherally around the sensor neutral axis at an interval of 120°, to measure the lateral forces applied to the sensor cap. The ends of the three peripheral FBG-inscribed optic fibers are fixed at the mounting holder and the optical fiber fixture, which are welded to the sensor flexure. To avoid chirping failure and low repeatability the prestressing forces are applied *a priori* to all the four optic fibers. The flexure structure is a nitinol tube. Nitinol alloy (75 Gpa) is used here due to its properties of low Young's modulus, super-elasticity and biocompatibility. It is frequently used in medical instruments [20], [23]. Generally, the stiffness of the nitinol tube in the axial direction is much greater than that in the lateral. To generate the same sensitivity in the both directions, the stiffness of the axial direction should be as same as that in the lateral. To this end, the upper segment of the nitinol tube is notched by laser machining, and the dimension and number of the slots and beams on the tube are designed deliberately. The sensor cap is designed to be hemispherical to

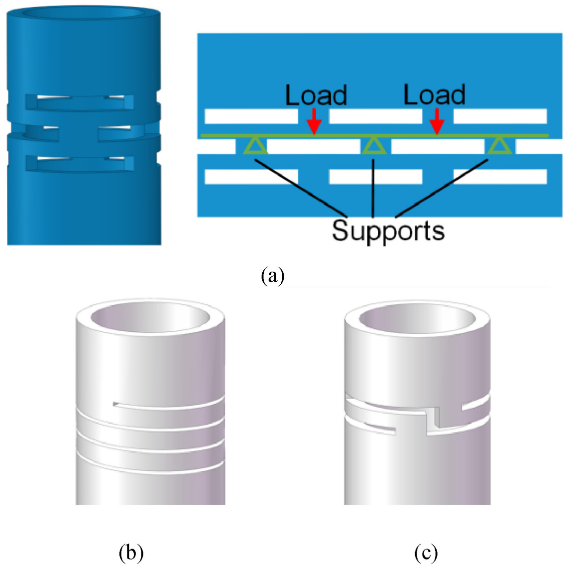

Fig. 2. Three concept Designs for the sensor flexure structure. (a) Design-1, multilayer continuous beams; (b) Design-2, helical spring; (c) Design-3, cantilever beams;

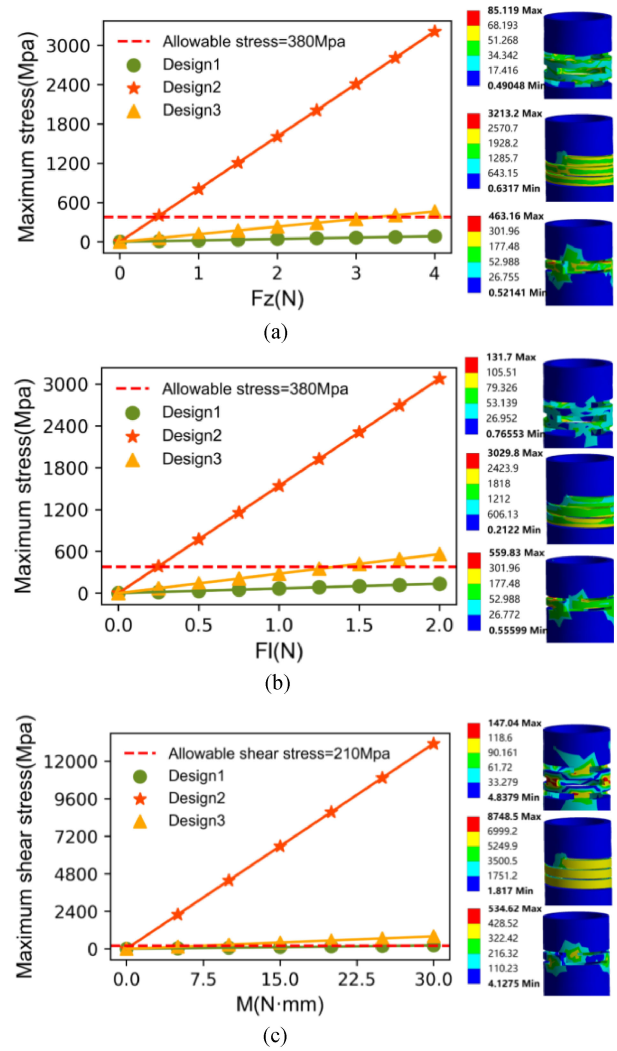

Fig. 3. FEA simulation results. (a) Left: the maximum stress vs the axial forces; Right: the stress contours with a 4 N axial force applied; (b) Left: the maximum stress vs the lateral forces; Right: the stress contours as 2 N lateral force is applied; (c) Left: the maximum shear stress vs the torsional moment. Right: the stress contours with a 20 N·mm torsional moment applied.

help the flexible ureteroscope move smoothly along the urinary tract. It is glued with the flexure structure so that the forces applied to the cap are able to transmit to the FBGs. The optical fiber fixture is a connecting block with four through-holes. One of the holes is the passage of the central optical fiber to the sensor cap, and the other three holes are used to glue the three peripheral optical fibers. The mounting holder is attached into the working channel of flexible ureteroscope, and through the channel the four FBG-inscribed optical fibers are led out the flexible ureteroscope and connected to an interrogator. This sensor configuration avoids the mutual crosstalk in the axial and lateral directions, which will be validated in the next section.

C. FEA for Flexure Optimization

What configuration should be chosen to design the flexure? What strain distribution occurs? When it comes to optimizing the flexure parameters, finite element analysis is often the first choice. Here the optimization is done with Ansys Workbench tool (ANSYS Inc., Pennsylvania). As mentioned previously, the notched flexure modulates the lateral and axial stiffnesses to achieve the same resolution in the two directions and to mitigate the force crosstalk. Three flexure structures are taken for comparison study. The first design concept, namely Design-1, uses parallel slots shown in Fig. 2(a), equivalent to continuous beams used in bridge design. Three supports are uniformly distributed to form the second layer at an interval of 120°around the flexure's central axis. From mechanics point of view, the three supports provide a stable triangular configuration. Design-2 of Fig. 2(b) works like a helical spring. It has high elasticity but cannot provide uniform stiffness in the lateral directions, namely x and y axes. Design-3 of Fig. 2(c) functions as cantilever beams. It is easy to fabricate but the peripheral FBGs cannot obtain the same sensitivity and resolution due to the nonsymmetric configuration.

Figure 3 gives the simulation results of the design concepts. The right side of the figure shows the stress contours as axial or lateral force, or torsion is applied to the sensor cap, respectively. The left side of Fig. 3(a) and (b) respectively shows the correlation of the maximum stress and the axial and lateral force, while in Fig. 3(c) it depicts the relationship of the maximum shear stress with respect to the applied torsional moment. It can be found that the elasticity of Design-2 is far higher than those of Design-1 and 3. Moreover, only in Design-1 the maximum stresses and the maximum shear stress are under the safe thresholds (the red dotted lines) within the force or moment allowed to apply to the sensor. Therefore, Design-1 was chosen due to its appropriate elasticity and symmetry against bending and torsion. Moreover, it is easy to adjust the axial stiffness

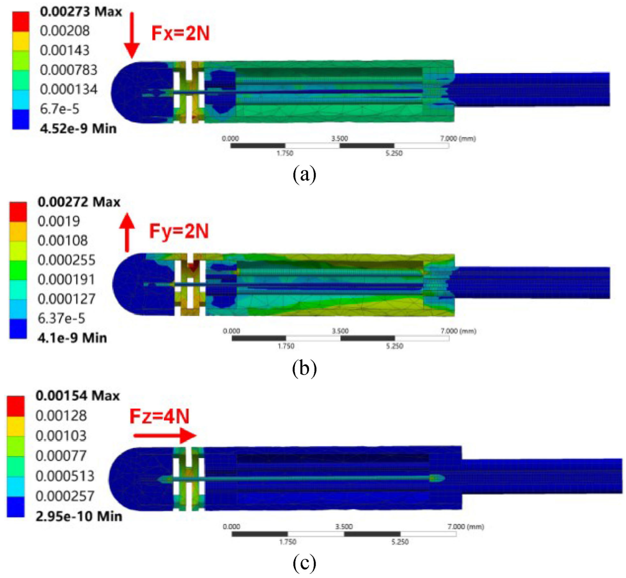

Fig. 4. Strain contours of force sensor. (a) 2 N in the x-direction; (b) 2 N in the y-direction; (c) 4 N in the axial direction.

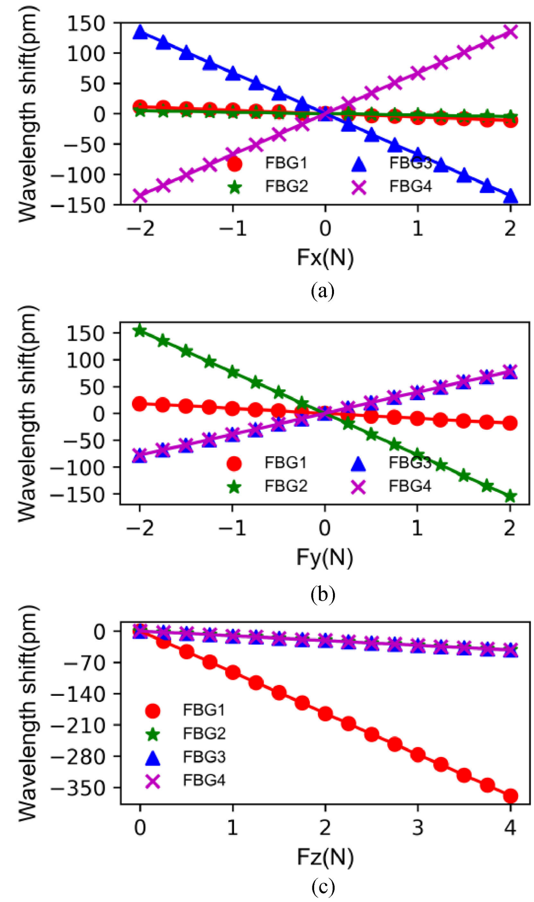

Fig. 5. The Bragg wavelength shifts of FBG1-4 vs the forces. (a) F_x; (b). F_y; (c) F_z.

through the flexure structure parameters. Figs. 4 and 5 show respectively the strain contours of the flexure of Design-1 and the FBG wavelength shift as force is applied to the sensor in the x, y, or z direction. It can be seen from Fig. 5 that the change of the wavelength shift of FBG1 is much larger than those of the other three as a force is applied to the sensor in z direction, while the inverse change tendency occurs in the lateral direction as forces are applied in the x or y direction, respectively. Therefore, Design-1 is able to alleviate considerably the crosstalk problem of the axial and lateral forces.

The four FBGs we use are modulated by the notched flexure. When a force is applied to the sensor tip, the flexure stretches or compresses the four FBG-inscribed optic fibers, resulting in the Bragg wavelength shifts. Making use of these shifts the force applied can thus be computed. Generally, the force sensor performance is characterized with measuring range, resolution and isotropy. These resultant properties largely are related to the flexure design. In addition, the sensing safety should be considered. To address this issue, a safety factor is introduced, and it is computed by the ratio of the maximum test force and the specified force. If the factor is greater than 1, it means that the flexure is safe under the maximum force load, otherwise the structural failure may occur. During the finite element analysis, the force sensor we design works well under a test force of up to 20 N in the axial direction, and a maximum force 5.5 N in the lateral direction. Hence, the safety factor of the flexure is 5 in the axial direction, and is nearly 3 in the lateral direction. Both directions completely meet the demand of the safe threshold. Moreover, there is no structural failure for the sensor to work under a maximum torsion of 27 N·mm now that the safety factor of shear stress is over 1.

The sensor sensitivity is the Bragg wavelength shift caused by a unit force. A sensitivity matrix $\boldsymbol{S}$ will be derived in Section III and further discussed in Section IV. Since it will be used in the following definition of other properties, it is computed from the simulation data and given *a priori* by

$$\boldsymbol{S} = \begin{bmatrix} -5.57 & -9.20 & -92.16 \\ -2.41 & -77.10 & -10.63 \\ -67.41 & 39.12 & -10.63 \\ 67.41 & 39.12 & -10.63 \end{bmatrix} \tag{1}$$

The sensitivity of the force sensor is relevant to the FBG interrogator as well. Here, the resolution of the interrogator we use is 1 pm. Hence the force senor has a sensitivity of 94 pm/N and a resolution of 0.01 N in the axial direction. They are computed from (1), (26)–(28) of Section IV. Similarly, the sensitivity and resolution in the lateral directions, namely the x and y axes, can be also obtained from these equations, and are the same as each other due to the symmetry of the flexure. The sensitivity in any lateral direction is 95 pm/N, and the resolution is 0.01N. The sensitivity or resolution of the sensor in the axial and lateral directions are nearly same.

Force isotropy is another sensor property which indicates the force distribution in all the directions. It is quite important for multiaxial sensors. When a force sensor is isotropic, it provides the most detailed data and high accuracy even though there exists interference noise or error in the sensitivity matrix. It is defined by the condition number of the sensitivity matrix S, namely,

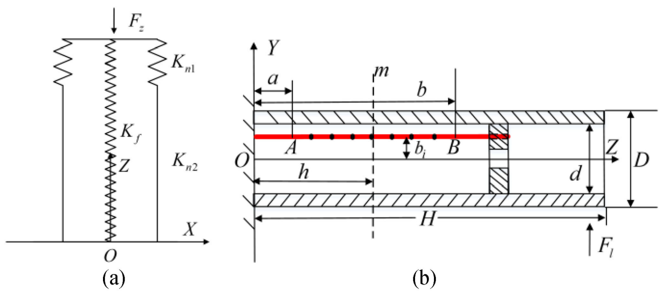

Fig. 6. Equivalent models of force sensor. (a) spring model in the axial direction; (b) cantilever beam model in the lateral direction.

$cond_p\ (\boldsymbol{S}) = \|\boldsymbol{S}\|_p \ \cdot \|\boldsymbol{S}^{-1}\|_p$. If it is close to 1, it means the sensor is isotropic. The condition number of the devised sensor can be computed from (1) and mostly it is close to 1. Hence, the isotropy of the devised sensor is excellent.

III. Force Decoupled Model

When axial force is applied to the FBG sensor, an equivalent spring model shown in Fig. 6(a) is used to derive the correlation of the flexure strain and the force. The stiffness of the upper portion of the flexure is represented by K_{n1}, and the lower one is denoted by K_{n2}. The latter is greater than the former, that is, $K_{n1} < K_{n2}$, because the upper portion of the flexure is notched. The stiffness of the optical fiber is taken into account as well and denoted by K_f. Then the resultant effective stiffness of the flexure K_{neff} can be computed by

$$K_{neff} = \ 1/\left(1/K_{n1} + 1/\left(K_{n2} + 3K_f\right)\right) + K_f \approx K_{n1} + K_f \tag{2}$$

and the strain of FBG1 can be given as follows

$$\varepsilon_1^z = \ 1/K_{neff} \cdot \ F_z = S_{F_z} \ \cdot F_z \tag{3}$$

where F_z represents the axial load and S_{F_z} is sensitivity constant. It indicates the linear relationship between the applied axial force F_z and the strain ε_1^z of FBG1.

To model the lateral force-strain relationship, the flexure is equivalent to a cantilever beam, and a coordinate system is established, as shown in Fig. 6. The z axis is aligned with the central line of the flexure. The y axis is parallel to the lateral direction and the x axis is perpendicular to the yz plane. The coordinate system is located at the fixed end of the cantilever beam. When a lateral force F_l is applied to the beam at the free end, the bending moment at the cross section m can then be calculated by

$$M\ (h) = F_l\ (H - h)\ \ (a \le h \le b) \tag{4}$$

where H is the height of the tube, h is the distance of the cross section m away from the origin of the cantilever beam, a and b are respectively the distances of the proximal and distal ends of FBG to the origin in the z axis.

Now let us analyze the strain and stress on the ith FBG (i = 1,2,3,4). Now that the notched flexure is a slender, long and nonuniform tube and its cross-sectional dimension is much smaller than its length, it is treated here as a Euler- Bernoulli beam [26], and the normal stress of the tube at cross section m can be thus computed by

$$\sigma_i\ (h) = \ M\,(h)\,b_i/I \tag{5}$$

where b_i is the radial distance of the ith FBG to the neutral line of the flexure, I is the inertia moment of the tube and given by

$$I \ = \ \pi\left(D^4 + d^4\right)/64 \tag{6}$$

where D and d are the outer and inner diameters of the tube.

The distance variable b_i can be calculated by

$$b_i = \begin{cases} 0, & i = 1 \\ \sqrt{x_i^2 + y_i^2} \cdot \cos\left(\theta - arctan\left(y_i/x_i\right)\right), & i = 2,\ 3,\ 4 \end{cases} \tag{7}$$

where $(x_i,\ \ y_i)$ is the coordinate of the ith FBG in the xy plane, and θ is the angle of the positive x axis and the force vector F_l.

In terms of the Hooke law, the strain of the ith FBG at the cross section m is derived from equations (4)-(7), given by

$$\begin{aligned} \varepsilon_i^l\,(h)\ \ &= \sigma_i\ (h)\,/E \ = \ M\,(h)\,b_i/\ (EI) \\ &= b_i\ (H - h)\,/K_b \cdot F_l \\ &(a \le h \le b) \end{aligned} \tag{8}$$

where E is the Young's modulus of the nitinol, and $K_b = \ EI$ is the bending stiffness.

Then, the resultant strain on the ith FBG can be computed by integrating (8) over the interval of $[a,\ b]$, which yields

$$\varepsilon_i^l = \ 2b_i\,(b - a)\,[2H - (a + b)]\,/K_b \cdot F_l \tag{9}$$

Now, the lateral force F_l is resolved to two components in the x and y axes, given by

$$F_x = F_l\ \cos\theta \tag{10}$$

$$F_y = F_l\ \sin\theta \tag{11}$$

Then, the correlation of the strain of the ith FBG and the force is established by

$$\varepsilon_1^l = \ 0 \tag{12}$$

$$\varepsilon_2^l = S_{F_{l2}} \ \cdot F_y \tag{13}$$

$$\varepsilon_3^l = S_{F_{l3}}\ \cos\left(\pi/6\right) \cdot F_x - S_{F_{l3}}\sin\left(\pi/6\right) \cdot F_y \tag{14}$$

$$\varepsilon_4^l = \ \ - S_{F_{l4}}\sin\left(\pi/6\right) \cdot F_x - S_{F_{l4}}\cos\left(\pi/6\right) \cdot F_y \tag{15}$$

where $S_{F_{li}}$ are sensitivity constants, and given by

$$S_{F_{li}} = \ 2\sqrt{x_i^2 + y_i^2}\,(b - a)\,[2H - (b + a)]\,/K_b$$

Equations (12)-(15) describe the linear correlation between the lateral force F_l and the strain of ith FBG, and the lateral forces has no crosstalk with FBG1 since $b_1 = \ 0$.

The strain and temperature changes cause the wavelength shift of Bragg grating, which is defined to be a linear function as [19]

$$\begin{aligned} \Delta\,\lambda_B = \ 2n\Lambda\,&\Big[\left\{1 - \left[n^2/2\right]\left[P_{12} - v\left(P_{11} + P_{12}\right)\right]\right\}\varepsilon \\ &+ \left(\alpha + \frac{dn/dT}{n}\right)\Delta T\Big] \end{aligned} \tag{16}$$

where $\Delta\lambda_B$ is the wavelength shifts of Bragg grating, Λ is the grating spacing, ε is the strain applied, P_{11}, P_{12} are the optic coefficients, α is the coefficient of thermal expansion, v is the Poisson ratio, n is the refractive index of the core, and ΔT is the temperature change.

Due to the difference of the room and body temperatures, the FBG temperature changes as the sensor goes into and out of human body. However, once the sensor enters into urinary tract, the change decreases quickly, and the wavelength shift caused by temperature is negligible. Hence, (16) is simplified and rewritten as

$$\Delta\,\lambda_{\mathrm{B}} = S_{\varepsilon}\ \cdot \varepsilon \tag{17}$$

where S_{ε} is constant coefficient.

Using (3), (13)–(15) and (17), the linear relationship of the force components F_x, F_y, F_z and the FBG wavelength shifts can be established by

$$\Delta\,\boldsymbol{\lambda_B} = \ \boldsymbol{S}\cdot\boldsymbol{F} \tag{18}$$

where $\boldsymbol{S}$ is the sensitivity matrix, given by

$$\boldsymbol{S}\ = \begin{bmatrix} 0 & 0 & S_{\varepsilon}S_{F_z} \\ 0 & S_{\varepsilon}S_{F_{l2}} & 0 \\ S_{\varepsilon}S_{F_{l3}}\cos(\pi/6) & -S_{\varepsilon}S_{F_{l3}}\sin(\pi/6) & 0 \\ -S_{\varepsilon}S_{F_{l4}}\sin(\pi/6) & -S_{\varepsilon}S_{F_{l4}}\cos(\pi/6) & 0 \end{bmatrix} \tag{19}$$

If $\boldsymbol{S}$ is known, the force then can be computed from (18). However, it is a class of overdetermined linear equation system. $\Delta\boldsymbol{\lambda}_{\mathrm{B}}$ represents the input, and $\boldsymbol{F}$ is the output of the linear system. This class of equation system is difficult to solve. If there exists a solution, it excessively depends on the condition number of the sensitivity matrix, $cond_p\,(\boldsymbol{S}) = \|\boldsymbol{S}\|_p\ \cdot \|\boldsymbol{S}^{-1}\|_p$. It is defined to determine if $\boldsymbol{S}$ is ill-conditioned or not. If it is ill-conditioned, a small change of $\boldsymbol{S}$ will lead to a considerable error or even wrong solution, and thus seriously deteriorates the accuracy of the FBG force sensor. In practice, the machining error and the sensor assembling deflection inevitably causes the disturbance of the matrix $\boldsymbol{S}$.

Hence, the SVD algorithm is chosen here to solve the force of (18). It can solve a linear overdetermined system accurately with minimal run time even though the matrix $\boldsymbol{S}$ is ill-conditioned or singular [27]. So, (18) is first decomposed into

$$\Delta\,\boldsymbol{\lambda_B} = \boldsymbol{U}\begin{bmatrix}\boldsymbol{\Sigma_r} \\ 0\end{bmatrix}\boldsymbol{V^T}\cdot\boldsymbol{F} \tag{20}$$

where $\boldsymbol{U}_{4\times4}$and $\boldsymbol{V}_{4\times4}$ are two orthogonal matrices, and $\boldsymbol{\Sigma_r}$ is a diagonal matrix.

$\boldsymbol{U}$ is further written to be

$$\boldsymbol{U}\ = [\boldsymbol{U_r},\, \bar{\boldsymbol{U}}] \tag{21}$$

where $\boldsymbol{U_r}$ is the first three columns of $\boldsymbol{U}$ and $\bar{\boldsymbol{U}}$ is the fourth column of $\boldsymbol{U}$.

We then have

$$\begin{aligned}\|\boldsymbol{SF} - \Delta\boldsymbol{\lambda_B}\|_2^2 &= \|\boldsymbol{\Sigma V^T F} - \boldsymbol{U}_r^T\Delta\boldsymbol{\lambda_B}\|_2^2\ + \|\bar{\boldsymbol{U}}^T\Delta\boldsymbol{\lambda_B}\|_2^2 \\ &\geq \|\bar{\boldsymbol{U}}^T\Delta\boldsymbol{\lambda_B}\|_2^2 \end{aligned} \tag{22}$$

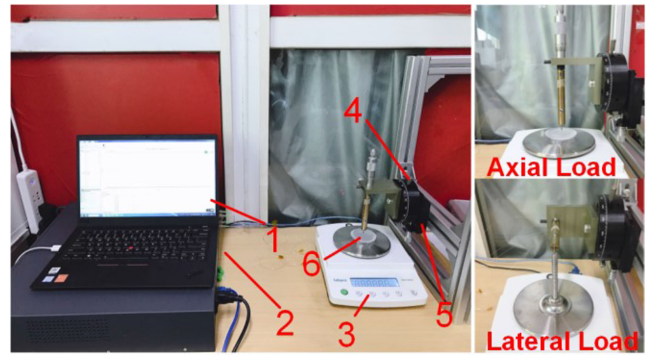

Fig. 7. The calibration platform. 1 laptop, 2 interrogator, 3 digital scale, 4 rotation stage, 5 linear translation stage, 6 gelatin.

If and only if

$$\boldsymbol{\Sigma V}^T\boldsymbol{F} - \boldsymbol{U}_r^T\Delta\,\boldsymbol{\lambda_B} =\ 0 \tag{23}$$

(22) can be established, and $\boldsymbol{F}$ is computed by

$$\boldsymbol{F}\ = \left(\boldsymbol{\Sigma V}^T\right)^{-1}\boldsymbol{U}_r^T\Delta\,\boldsymbol{\lambda_B} = \ \boldsymbol{V\Sigma}^{-1}\boldsymbol{U_r^T}\Delta\boldsymbol{\lambda_B} \tag{24}$$

IV. Experimental Results

To compute the force applied to the sensor from the Bragg wavelength shifts, the sensitivity matrix $\boldsymbol{S}$ has to be obtained *a priori* by sensor calibration. The calibration platform shown in Fig. 7 is used. It consists of the sensor prototype to be calibrated, a laptop computer, an FBG interrogator, a high-precision digital scale, and a micrometer head which is fixed on a mounting bracket through linear translation and rotation stages. The force sensor is fixed by the micrometer head through a metal jig. During calibration the room temperature is presumed to be constant. The force at the tip of the sensor is tuned through the linear stage, the rotary stage and the micrometer, and the force data is generated by the digital scale. The wavelength shifts of the sensor's FBGs are acquired by the interrogator. Both the force and wavelength shift data are recorded simultaneously by computer. The forces in the *x*, *y*, and *z* directions are separately applied to the sensor prototype. In the axial direction, the force is changed from 0 to 4 N, and then reduced from 4 N to 0 N at an interval of 0.2 N. In the lateral directions, the force is changed from -2 N to 2 N at the same interval as the axial direction. Three tests have been done for each experiment, and the average values of the force and the wavelength shift are used in calibration to reduce the data noise.

A. Calibration and Model Validation

With these force and wavelength shift data, (18) is obtained by the least-squares method, given by

$$\begin{bmatrix}\Delta\lambda_{B1}\\ \Delta\lambda_{B2}\\ \Delta\lambda_{B3}\\ \Delta\lambda_{B4}\end{bmatrix} = \begin{bmatrix} -20.80 & -0.63 & 70.38 \\ -22.26 & -79.37 & 2.68 \\ -111.25 & 27.78 & -1.10 \\ 111.44 & 37.85 & 3.55 \end{bmatrix}\begin{bmatrix}F_x\\ F_y\\ F_z\end{bmatrix} \tag{25}$$

So far, the sensitivity matrix $\boldsymbol{S}$ has been obtained. As discussed previously, the SVD algorithm is used to solve the

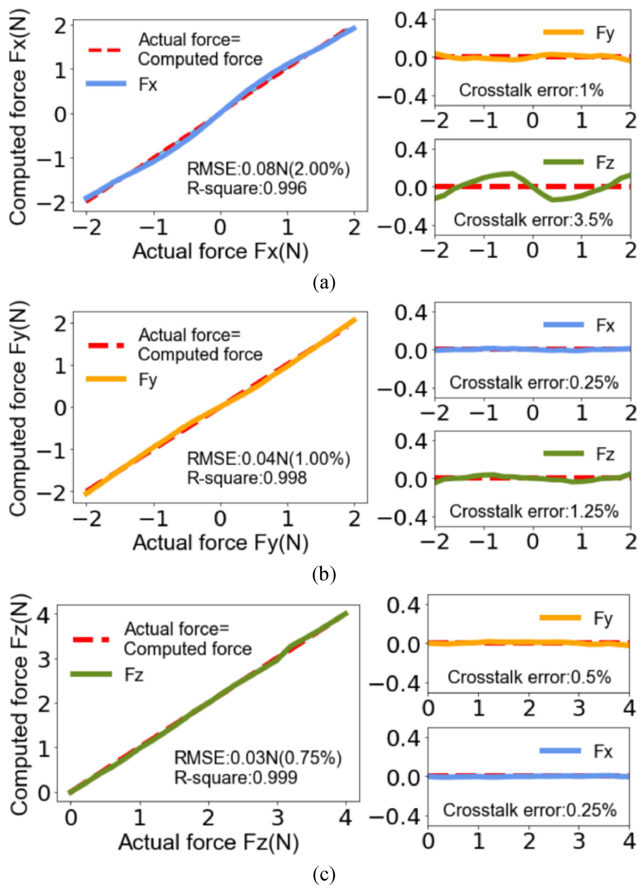

Fig. 8. Computed force versus actual force and crosstalk errors to other force components.

over-determined linear equations (25) and to yield the decoupled model. However, before it is used to compute the force components, the linear regression model should be validated in advance. Here, statistical methods are taken into account to verify the rationality and estimation accuracy of the model. To this end, we first introduce null hypothesis which assumes that the linear relationship between the force component and the wavelength shift is not established. To test the hypothesis, we then calculate the P-value from the computed forces according to the F-test of model significance. It is 0.03, less than the significance level 0.05, which means that the null hypothesis is false. Consequently, it does suggest the force components can be computed by the linear regression model.

Now let us examine the accuracy of the linear decoupled model. Fig. 8 shows the computed forces vs the actual forces. It can be seen that the slopes of the fitted lines are nearly 1, and the R-square value of F_x is 0.996, 0.998 for F_y, and 0.999 for F_z. These computed force components are very close to the values of the actual forces measured by the digital scale. The accuracy can be proved by the root mean square errors (RMSE) as well. The RMSE in the x direction is 0.06 N (2%), 0.06 N (1%) in the y direction and 0.08 N (0.75%) in the z direction. Furthermore, from the right side of Fig. 8, the 3-axis force components of the sensor have very little crosstalk to each other.

B. Sensor Performance

The performance of the devised sensor including sensitivity, resolution, accuracy, repeatability and hysteresis, is assessed with the force data acquired. Now let us discuss them below.

1) Sensitivity: The matrix $\mathbf{S}$ of (19) is now written to be three components $[\mathbf{S}_1, \mathbf{S}_2, \mathbf{S}_3]$, and with (25) we then have the sensitivity of the force sensor in the three directions, given by

$$S_x = \|\boldsymbol{S}_1\|_2 = \sqrt{S_{11}^2 + S_{21}^2 + S_{31}^2 + S_{41}^2} = 160 \text{ pm/N} \tag{26}$$

$$S_y = \|\boldsymbol{S}_2\|_2 = \sqrt{S_{12}^2 + S_{22}^2 + S_{32}^2 + S_{42}^2} = 92 \text{ pm/N} \tag{27}$$

$$S_z = \|\boldsymbol{S}_3\|_2 = \sqrt{S_{13}^2 + S_{23}^2 + S_{33}^2 + S_{43}^2} = 71 \text{ pm/N} \tag{28}$$

where S_x, S_y and S_z are the sensor sensitivities in the x, y and z axes, respectively.

2) Resolution: The sensor resolution defines its smallest absolute amount of force change. As mentioned previously, this change is related to the interrogator we use. Its resolution is 1 pm. The resolutions of the devised sensor in the x, y and z direction are 0.006 N, 0.011 N, and 0.014 N, respectively.

3) Accuracy: Accuracy specifies the amount of uncertainty in a measurement with the force sensor. It is defined to be the difference of a measured force value with respect to an absolute standard. The root mean squared error (RMSE) is frequently used to demonstrate the accuracy. With the experimental data measured by the devised sensor, the RMSEs of the sensor in the x, y, and z directions are 0.08 N (2%), 0.04 N (1%), and 0.03 N (0.75%), respectively.

4) Repeatability: Repeatability indicates the consistency of the multiple measurement results under the same condition. To some extent it proves the reliability of the sensor. Fig. 9 shows the sensor data of three tests, and yields the repeatability errors of the sensor in the x, y and z axes. They are $\pm 1.50\%$, $\pm 1.50\%$, and $\pm 2.0\%$, computed by

$$r_{R_j} = \pm\left(\Delta R_{j_{max}} / F_{R_j}\right) \times 100\% \; j = x, y, z \tag{29}$$

where F_R is the measurement range of force, and $\Delta R_{j_{max}}$ is the maximum deviation.

5) Hysteresis: Hysteresis occurs as a force is increasingly applied to the sensor from 0 to the maximum and then unloaded to 0. It is defined to be the ratio of the maximum force deviation between the loading and unloading tests over the measurement range, that is

$$R_{H_j} = \pm\left(\Delta H_{j_{max}} / F_{R_j}\right) \times 100\% \; j = x, y, z \tag{30}$$

where $\Delta H_{j_{max}}$ is the maximum deviation of the two tests in each axis.

With the test data of Fig. 10, the hysteresis of the devised sensor in the x, y or z axis can be computed from (30). They are $\pm 0.50\%$, $\pm 0.75\%$, and $\pm 0.75\%$, validating the high resilience of the sensor structure.

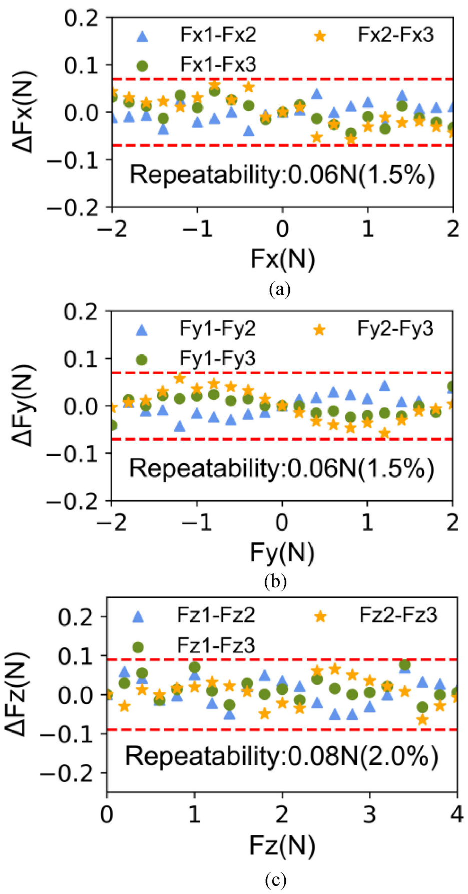

Fig. 9. The measuring repeatability in the different directions: (a) F_x; (b) F_y; (c) F_z.

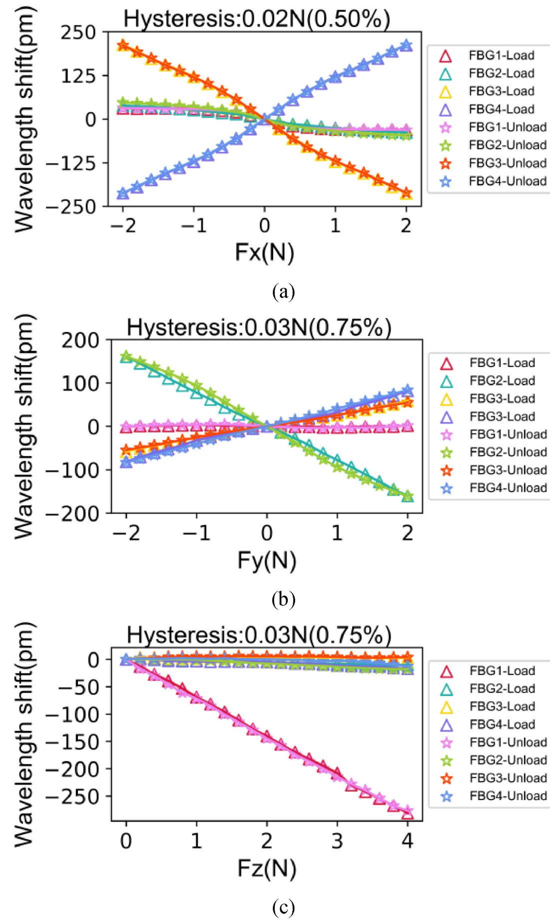

Fig. 10. Hysteresis performances of force sensor in different directions. (a) *X*-direction. (b) *Y*-direction. (c) *Z*-direction.

TABLE II
THE PERFORMANCE OF SENSOR

	X	*Y*	*Z*
Force range	[-2 N 2 N]	[-2N 2N]	[0 4 N]
Sensitivity	160 pm/N	92 pm/N	71 pm/N
Resolution	0.006 N(0.15%)	0.011 N(0.28%)	0.014 N(0.35%)
R-square	0.996	0.998	0.999
Accuracy	0.08 N(2.00%)	0.04 N(1.00%)	0.03 N(0.75%)
Repeatability errors	0.06 N(1.50%)	0.06 N(1.50%)	0.08 N(2.00%)
Hysteresis	0.02 N(0.50%)	0.03 N(0.75%)	0.03 N(0.75%)

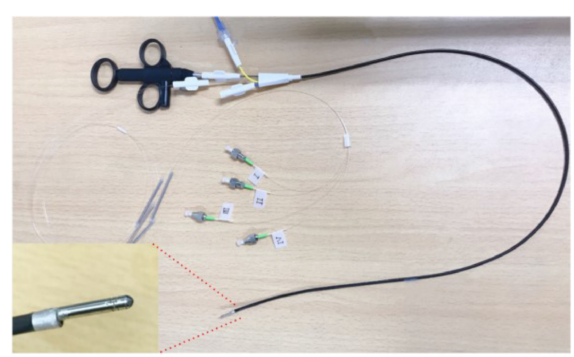

Fig. 11. A flexible ureteroscope with a force sensor prototype.

The devised sensor is characterized by the above properties, which are summarized in Table II. It can be noticed that the sensor linearity is pretty well, close to 1, and its measurement error is less than 2%. Although there have repeating errors and hysteresis, the sensor performance is robust and stable, and can accurately measure the force applied to the sensor tip.

C. Force Signal Analysis

During a ureteroscope lithotripsy, the flexible ureteroscope advances from the bladder orifice and accesses into the kidney calyces through the spontaneous urinary track, and its tip contacts occasionally the wall of the ureteral tract or calculi stone. The contact force is critical for the ureteroscopy safety and should be under control. To this end, the fiber optic sensor devised is attached to the tip of a flexible ureteroscope, shown in Fig. 11. Pilot tests have been done to examine the competence of this sensor to accurately measure the contact force and the capability to discriminate different objects at the sensor tip from the measured force. Two sorts of objects are chosen to test the force sensor, namely soft silica gel and pebble stone. Fig. 12 shows the force signals measured. It can be seen that the force

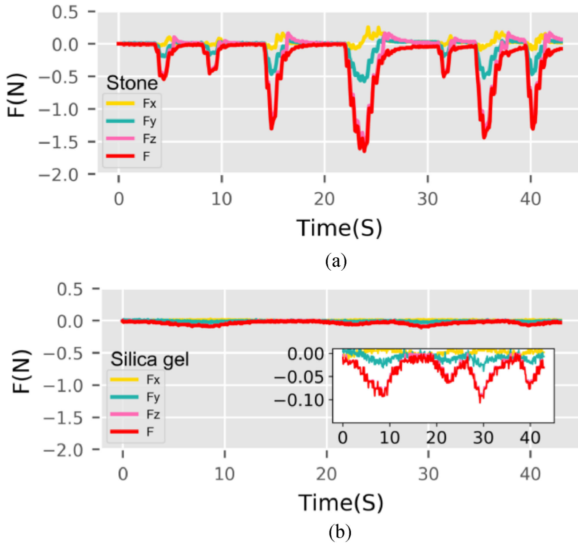

Fig. 12. Force responses at the tip of ureteroscope. (a) stone; (b) soft silica gel.

generated as the tip of the ureteroscope hits a pebble stone is much larger than that in the silica gel [28].

V. Conclusion

In this paper, a miniature triaxial fiber optic force sensor is devised with four FBGs to measure the force at the tip of a flexible ureteroscope. First, a notched flexure with multilayer continuous beams is designed to modulate the axial and lateral stiffnesses of the sensor and eliminate the mutual crosstalk of force components. Second, the flexure structure parameters are optimized by the FEA method to accommodate to the sensor performance and miniaturization while ensuring its safety and isotropy. Third, a decoupled model based on SVD algorithm is proposed to compute the force components in terms of the FBG wavelength shifts, even though the sensitivity matrix $\boldsymbol{S}$ is ill-conditioned. Finally, experiments have been done to calibrate the force sensor and to assess its performance, and show that the sensor is able to provide the measurement range, resolution, accuracy and sensitivity. The repeatability and hysteresis properties of the sensor validate its reliability and robustness. Furthermore, pilot tests show the capability of the sensor to discriminate the different objects at the tip of a ureteroscope. The interference could be problematic as the ureteroscope moves in the DYNAMIC fluid. A solution to the problem is to isolate the disturbance signal from the sensor signal through a filter. Silicone rubber block is also a solution, as done in [22]. We will investigate the influence of fluid dynamics on the FBG sensor in the future in-vivo experiments.

References

[1] H. Heers and B. W. Turney, “Trends in urological stone disease: A 5-year update of hospital episode statistics,” *BJU Int.*, vol. 118, pp. 785–789, 2016.

[2] K. Taguchi *et al.*, “The urological association of asia clinical guideline for urinary stone disease,” *Int. J. Urol.*, vol. 26, pp. 688–709, 2019.

[3] R. M. Geraghty *et al.*, “Worldwide trends of urinary stone disease treatment over the last two decades: A systematic review,” *J. Endourol.*, pp. 1–24, 2016.

[4] B. H. Eisner *et al.*, “Ureteroscopy for the management of stone disease,” *Nat. Rev. Urol.*, vol. 7, no. 1, pp. 40–55, Jan. 2010.

[5] J. J. Rassweiler *et al.*, “Future of robotic surgery in urology,” *BJU Int.*, vol. 120, pp. 822–841, 2017.

[6] Z. Tokatli *et al.*, “Determination of the learning curve of robotic flexible ureterorenoscopy,” *J. Urol.*, vol. 191, no. 4, pp. 1092–1100, Jun. 2014.

[7] R. Saglam *et al.*, “A new robot for flexible ureteroscopy: Development and early clinical results (ideal stage 1-2b),” *Eur. Urol.*, vol. 66, pp. 1092–1100, Jun. 2014.

[8] W. Lai *et al.*, “An integrated sensor-model approach for haptic feedback of flexible endoscopic robots,” *Ann. Biomed. Eng.*, vol. 48, no. 4, pp. 342–356, 2020.

[9] C. Alleblas *et al.*, “Performance of a haptic feedback grasper in laparoscopic surgery: A randomized pilot comparison with conventional graspers in a porcine model,” *Surg. Innov.*, vol. 26, no. 5, pp. 573–580, 2019.

[10] A. L. Trejos *et al.*, “Design and evaluation of a sterilizable force sensing instrument for minimally invasive surgery,” *IEEE Sensor J.*, vol. 17, no. 13, pp. 3983–3993, Jul. 2017.

[11] M. Kalantari *et al.*, “A piezoresistive tactile sensor for tissue characterization during catheter-based cardiac surgery,” *Int. J. Med. Robot. Comput. Assist. Surg.*, vol. 7, no. 4, pp. 41–440, 2011.

[12] Y. Noh *et al.*, “Image-based optical miniaturized three-axis force sensor for cardiac catheterization,” *IEEE Sensor J.*, vol. 16, no. 22, pp. 7924–7932, Nov. 2016.

[13] U. Kim *et al.*, “A surgical palpation probe with 6-axis force/torque sensing capability for minimally invasive surgery,” *IEEE Trans. Ind. Electron.*, vol. 65, no. 3, pp. 2755–2765, Mar. 2018.

[14] P. Panagiotis *et al.*, “MRI-compatible intensity-modulated force sensor for cardiac catheterization procedures,” *IEEE Trans. Biomed. Eng.*, vol. 58, no. 3, pp. 721–726, Mar. 2011.

[15] P. Polygerinos *et al.*, “Triaxial catheter-tip force sensor for mri-guided cardiac procedures,” *IEEE/ASME Trans. Mechatronics*, vol. 18, no. 1, pp. 386–396, Feb. 2013.

[16] Z. Mo and W. Xu, “Temperature-compensated optical fiber force sensing at the tip of a surgical needle,” *IEEE Sensor J.*, vol. 16, no. 24, pp. 8936–8943, Dec. 2016.

[17] T. W. Yang *et al.*, “Identification of tissue types and boundaries with a fiber optic force sensor,” *Sci. China-Inf. Sci.*, vol. 57, pp. 8215–8223, Dec. 2014.

[18] L. Xuan *et al.*, “Miniature fiber-optic force sensor based on low- coherence Fabry-Perot interferometry for vitreoretinal microsurgery,” *Biomed. Opt. Express*, vol. 3, no. 5, pp. 5, Apr. 2012.

[19] D. Krohn *et al.*, *Fiber Optic Sensors: Fundamentals and Applications*, 4th ed., Bellingham, WA USA: SPIE Press, 2014, pp. 63–77.

[20] X. He *et al.*, “A sub-millimetric 3-DOF force sensing instrument with integrated fiber Bragg grating for retinal microsurgery,” *IEEE Trans. Biomed. Eng.*, vol. 61, no. 2, pp. 522–534, Feb. 2014.

[21] T. Li *et al.*, “Three-dimensional catheter distal force sensing for cardiac ablation based on fiber bragg grating,” *IEEE/ASME Trans. Mechatronics*, vol. 23, no. 5, pp. 2316–2327, Oct. 2018.

[22] T. Li, A. Pan, and H. Ren, “A high-resolution tri-axial catheter-tip force sensor with miniature flexure and suspended optical fibers,” *IEEE Trans. Ind. Electron.*, vol. 67, no. 6, pp. 5101–5111, 2020.

[23] A. Gao *et al.*, “Fiber bragg grating based triaxial force sensor with parallel flexure hinges,” *IEEE Trans. Ind. Electron.*, vol. 65, no. 10, pp. 8215–8223, Oct. 2018.

[24] T. Tefik *et al.*, “Impact of ureteral access sheath force of insertion on ureteral trauma: In vivo preliminary study with 7 patients,” *Ulus Travma ve Acil Cerrahi Dergisi*, vol. 24, no. 6, pp. 514–520, Nov. 2018.

[25] K. Kaler *et al.*, “Initial clinical testing of ureteral access sheath force sensor to prevent ureteral injuries,” *Can Urol. Assoc.*, vol. 12, no. S87, May 2018.

[26] J. M. Gere and B. J. Goodno, *Mechanics of Materials*, 7th ed., Toronto, Canada: Cengage Learning, 2009, pp. 304–421.

[27] J. Kiusalaas, *Numerical Methods in Engineering with Python 3*. Cambridge, MA, USA: Cambridge Univ. Press, 2013, pp. 31–51.

[28] Y. N. Deng *et al.*, “Signal feature analysis of contact force at the tip of a flexible ureteroscope,” in *Proc. 42nd Annu. Int. Conf. IEEE Eng. Med. Biol. Soc.*, 2020.